Exact ab initio transport coefficients in bcc Fe–X (X = Cr, Cu, Mn, Ni, P, Si) dilute alloys

Luca Messina,[1,*] Maylise Nastar,[2] Thomas Garnier,[2,3] Christophe Domain,[4] and Pär Olsson[1]

[1] *KTH Royal Institute of Technology, Reactor Physics, 106 91 Stockholm, Sweden*
[2] *CEA, DEN, Service de Recherches de Métallurgie Physique, F–91191 Gif–sur–Yvette, France*
[3] *Department of Materials Science and Engineering, University of Illinois, Urbana–Champaign, Illinois 61801, USA*
[4] *Département Matériaux et Mécanique des Composants, EDF–R&D, Les Renardières, F–77250 Moret sur Loing, France*

(Dated: December 6, 2016)

Defect-driven diffusion of impurities is the major phenomenon leading to formation of embrittling nanoscopic precipitates in irradiated reactor pressure vessel (RPV) steels. Diffusion depends strongly on the kinetic correlations that may lead to flux coupling between solute atoms and point defects. In this work, flux coupling phenomena such as solute drag by vacancies and radiation induced segregation at defect sinks are systematically investigated for 6 bcc iron–based dilute binary alloys, respectively containing Cr, Cu, Mn, Ni, P and Si impurities. Firstly, solute–vacancy interactions and migration energies are obtained by means of ab initio calculations; subsequently, Self Consistent Mean Field theory is employed in order to determine the exact Onsager matrix of the alloys. This innovative multi-scale approach provides a more complete treatment of the solute-defect interaction than previous multifrequency models. Solute drag is found to be a widespread phenomenon that occurs systematically in ferritic alloys and is enhanced at low temperatures (as for instance RPV operational temperature), as long as an attractive solute–vacancy interaction is present, and that the kinetic modeling of bcc alloys requires the extension of the interaction shell to the second nearest neighbors. Drag occurs in all alloys except Fe(Cr); the transition from dragging to non–dragging regime takes place for the other alloys around (Cu, Mn, Ni) or above (P, Si) the Curie temperature. As far as only the vacancy–mediated solute migration is concerned, Cr depletion at sinks is foreseen by the model, as opposed to the other impurities which are expected to enrich at all temperatures (P, Ni) or below a rather high temperature (Si, Cu, Mn). The results of this study confirm the current interpretation of the hardening processes in ferritic–martensitic steels under irradiation.

INTRODUCTION

Solute diffusion in alloys is predominantly mediated by defect-driven mechanisms, that is through vacancy exchange and interstitial migration. Especially in irradiated materials, the defect concentrations can be considerably larger than in thermal equilibrium and solute diffusion can then be strongly enhanced or even induced. According to the binding or repulsive nature of the solute–point defect (PD) interaction, kinetic correlation effects can arise and coupled solute–PD fluxes can lead to an acceleration of thermodynamic–driven diffusion (radiation–enhanced effect) or to the net flux of solute atoms even in the absence of thermodynamic driving forces for the solute (radiation–induced effect). Flux coupling is of great importance in any metallurgical process in which an accurate microstructural characterization of the material is needed, as for instance in phase transformations during heat treatments [1, 2]. A precise description of the diffusion mechanisms is essential for a correct modeling of driven systems because both phase transitions and stationary states depend on the alloy diffusion properties. In addition, flux coupling is fundamental for understanding the nano– and microstructural evolution of irradiated materials. For instance, it plays a key–role in radiation induced segregation (RIS) of solute atoms at sinks. Recently, a systematic experimental RIS study of several irradiated ferritic–martensitic alloys in the low–temperature regime showed that many impurities consistently enrich at grain boundaries [3]. It is mentioned that this behavior can be explained in terms of balance between vacancy– and interstitial– mediated diffusion. This issue can be analyzed and solved if the transport coefficients (or Onsager matrix) of the system are known [4].

An important example of irradiated alloys is represented by reactor pressure vessels (RPV) steels, whose integrity is affected by the microstructural changes induced by the neutron–induced defect population. In particular, hardening and consequent embrittlement due to the formation of nanofeatures inside the steel is regarded as the most serious concern for the reactor lifetime. These nanofeatures consist of matrix damage (small voids and dislocation loops) or defect–impurity clusters. They originate from the PD produced by incident neutrons and their interaction with the alloy constituents. Both types of damage hinder the movement of dislocations and consequently increase the RPV ductile–to–brittle transition temperature (DBTT). In particular, Mn–Ni–Si–rich precipitates have been recently observed in RPV surveillance tests to be the cause of a further unexpected DBTT shift [5, 6]. Intergranular segregation of impurities like phos-

phorus is, among others, a secondary but non–negligible embrittling phenomenon occurring under irradiation [7]. The investigation of the phenomena inducing solute clustering even in undersaturated conditions has been carried on since the early stages of nuclear power plant operation, but is still missing an exhaustive explanation.

RPV–like steels are usually body–centered cubic (bcc) ferritic dilute alloys, with varying concentrations of Cu, Mn, Ni, Si, P, Cr and other minor impurities [8, 9]. Although they have been extensively studied, a systematic investigation of flux coupling is still missing. This work aims at covering this gap. The issue is tackled with model binary alloys, in order to identify the inherent transport properties of each solute species in bcc iron. Six alloys are selected for this purpose (Fe–X, with X=Cu, Mn, Ni, P, Si and Cr), in reference to the solute atoms that are usually observed in nanoclusters [5, 10]. In addition to those, Cr is of great interest mainly for the upcoming Generation IV reactor vessels and other structural materials, although in non–dilute concentrations.

A very small number of experimental studies are devoted to binary model alloys. The observation of irradiated iron dilute alloys seems to indicate that a strong kinetic correlation between vacancies and Mn, Si, Ni, Cu and P solute atoms is the trigger for solute–vacancy cluster agglomeration and accelerated void growth [11]. A strong kinetic correlation between PD and Mn solute atoms was also advanced as cause for the formation of Mn–rich clusters observed around dislocation loops [12, 13], and in such cases the contribution of vacancy versus interstitial diffusion is still to be determined.

Such issues can be properly assessed by computing the transport coefficients (L_{ij}). From these quantities, flux coupling between different atomic species can be easily inferred. In a near equilibrium system, the flux of each species can be written as

$$J_i = -\sum_{j=1}^{N} \frac{L_{ij}}{k_B T} \nabla \mu_j \,, \tag{1}$$

or in other words as a linear combination of the thermodynamic driving forces $\nabla \mu_j$ acting on all species, including PD. The Lij coefficients are therefore expressions of the kinetic response of the system to an external solicitation and allow for a clear separation between thermodynamic and kinetic properties of the alloy. Moreover, the off–diagonal coefficients $L_{ij,i\neq j}$ emphasize the kinetic coupling that may appear between fluxes of different atomic species, for instance between solvent and solute atoms, which would be missed by 'traditional' diffusion coefficients.

The Lij:s can be inferred from experimentally measured tracer diffusion coefficients with Darken's [14] or Manning's [15] theories, but none of them are able to provide an accurate estimation of the crucial off–diagonal coefficients, and systematically predict such coefficients to be positive. Alternatively, the Lij:s can be obtained starting from microscopic jump frequencies that can be computed either with interatomic potentials [16–18] or through density functional theory (DFT) calculations [19–22]. Such frequencies can be then used as parameters for atomistic Monte Carlo simulations [23] or analytical multifrequency models [24]. Monte Carlo simulations can be effective but become computationally demanding when complex solute–defect interactions are present. On the other hand, the analytical models developed in the so–called multifrequency framework that are available in the literature take into account only 1nn solute–vacancy interactions (SVI), or 2nn interactions to a partial extent [25, 26]. In the latter case, the flux coupling prediction capability is considerably hampered by strong approximations in the microscopic jump rates. Later on, a more general and flexible Self–Consistent Mean Field (SCMF) method was developed, initially for vacancy–mediated diffusion in concentrated ideal solid solutions [27], then in non–ideal alloys [28], and finally for interstitial diffusion [29, 30]. Its main advantage is to yield exact transport coefficients in dilute alloys; moreover, it can be extended to any range of solute–defect interactions, its self–consistency being ensured by an appropriate choice of the amount of unknowns. The reliability of the SCMF theory is assured by its perfect agreement with Monte Carlo simulations in generic AB alloys, for both vacancy– [28] and interstitial–mediated diffusion [29]. More recently, it was successfully employed to analyze the conditions for the onset of vacancy drag in bcc [31] and fcc [32] alloys. These works have highlighted the importance of the nearest neighbor (nn) shells beyond the first one for a correct prediction of flux coupling, as opposed to many studies where only 1nn interactions were considered [33, 34].

On the modeling side, flux coupling was investigated for the Fe(P) system by molecular dynamics simulations based on an interatomic potential [16]. In this case it was shown that a strong kinetic correlation with both vacancies and interstitials lets P migrate quickly to PD sinks. Furthermore, kinetic Monte Carlo (KMC) simulations of the Fe(Cu) system confirmed the possibility of Cu–vacancy drag at low temperatures. To the authors' knowledge, the only referenced case in which a full set of transport coefficients was derived for the Fe–X dilute alloys object of this work was a study on the Fe(Cr) and Fe(Ni) systems by Choudhury et al. [22]. They applied an approximated multifrequency model where 2nn SVI were only partially considered, and concluded that no solute drag was expected for either solute. Solute drag phenomena are known to be strongly related to attractive solute–vacancy binding energies. Calculations of such binding energies in Fe dilute alloys [35] corroborate this conclusion in Fe(Cr) alloy, but not in Fe(Ni). Indeed the prediction of no drag effect in Fe(Ni) is in contradiction with the idea that binding SVI at first and second nn sites lead to solute drag phenomena.

In this work, the SCMF method is applied to dilute ferritic alloys in order to provide an exact prediction of the flux coupling tendencies between solutes and defects. The Onsager matrix is computed for each of the selected dilute alloys from a set of DFT-computed jump frequencies. The obtained phenomenological coefficients are then used to discuss solute drag as function of temperature, to predict RIS tendencies and to obtain solute diffusion coefficients for the sake of comparison with experimental values. Only the case of vacancy mediated diffusion is considered, and the issue of interstitial mediated diffusion is left for a future work.

The paper is organized as follows. The following section is dedicated to the first principle computation of solute–vacancy interaction energies and jump frequencies. The focus is then moved to the mean field treatment of the obtained jump frequencies in the SCMF framework. Finally, the computed Lij:s, vacancy drag, diffusion coefficients and RIS tendencies are shown in the last section and are analyzed in terms of physical implications on the RPV microstructural evolution.

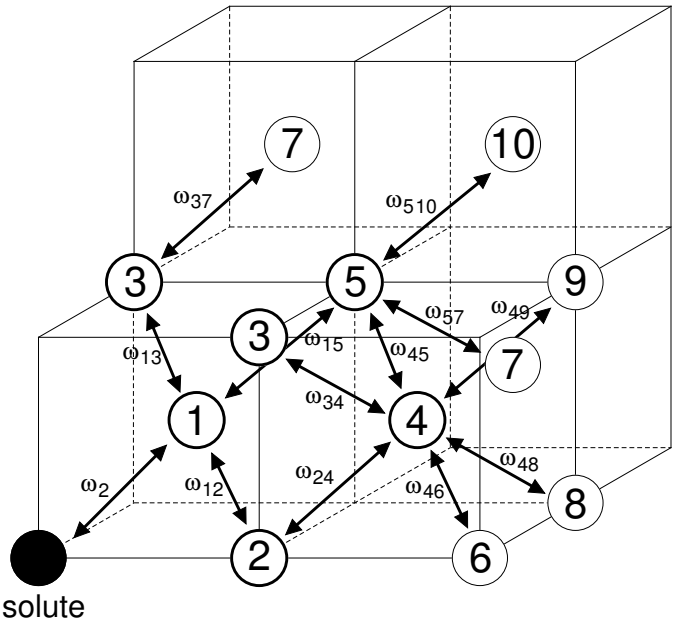

FIG. 1. Network of the 12 Fe-V jump frequencies affected by the presence of a solute atom, for solute–vacancy interactions extending to the 5nn distance. The solute–vacancy exchange is labeled with ω_2, while ω_0 represents the unaffected Fe-V jump frequency (not shown).

AB INITIO STUDY

Definition of jump frequencies

The phenomenological coefficients related to vacancy–mediated diffusion can be derived in terms of microscopic vacancy jump frequencies. These jump rates depend on the activation energy that is needed for one surrounding atom to move into a vacant site. In the framework of transition state theory, a jump frequency ω_{ij} for an atom moving from site j to a vacant site i is defined as [36]:

$$\omega_{ij} = \nu_{ij} \exp\left(-\frac{E_{ij}^{\mathrm{mig}}}{k_B T}\right) \quad . \tag{2}$$

The attempt frequency ν_{ij} is related to the lattice vibrational modes, whereas the energy barrier E_{ij}^{mig} depends on the type of moving atom and the local chemical environment around the moving atom-vacancy pair. In a binary dilute alloy, solvent and solute atoms are characterized by different migration barriers, and the corresponding jump frequencies are referred to as ω_0 and ω_2, in accordance to LeClaire's nomenclature [24]. Moreover, if a strong solute-vacancy interaction exists, the jump rates of the solvent atoms in the vicinity of the solute-vacancy pair are considerably affected.

The set of jump frequencies that need to be calculated depends on the spatial extent of the SVI. For instance, for bcc dilute alloys, Le Claire [24] showed that 4 jump types are needed if only the 1nn SVI is considered, or 9 jump types when the 2nn SVI is introduced. However, the 2nn analytical models derived from Le Claire's framework [25, 26] are approximated to such an extent that the flux coupling tendency is considerably underestimated, as explained in the following section.

In principle, nothing is limiting the spatial extent of the SVI, but in practice the range must be limited in order to have a finite set of jump frequencies. The choice of a cutoff distance depends not only on the extent of the SVI, but also on the kinetics of the targeted phenomenon: in the case of solute drag by vacancies, the paths leading to a possible drag mechanism are multifold and can involve distances beyond the 2nn position [31]. Moreover, some of the impurities of interest present a non-negligible SVI at the 5nn distance [37]. Hence, the interaction shell was extended in this work to 5nn sites, which entails the definition of 12 forward-backward jump types, as shown in Fig. 1.

Ab initio calculations based on DFT represent an accurate way of obtaining zero–temperature interaction energies, migration barriers and attempt frequencies. Finite–temperature effects, such as the influence of magnetic disordering on ω_{ij}, must be explicitly introduced in order to extrapolate the diffusion properties to higher temperatures, as was done for instance in [38]. Other approaches, such as the development of alloy interatomic potentials, can be pursued. Such potentials are however fitted either on ab initio data or experiments. Therefore, they are valid only for the specific system they were developed for and need a cutoff distance beyond which the interatomic interactions are set to null. On the other hand, in DFT calculations there is no assumption on the

potential range. Therefore, the SVI trends as function of nn distance must be investigated in order to estimate at which distance they become negligible.

Ab initio methodology

The first principle calculations in this work were performed with the Vienna ab initio simulation package (VASP) [39–41]. As part of the ab initio procedure, the supercell relaxation allowed for the determination of solute–vacancy binding energies, which represents a partial hint of whether a solute atom is likely to follow a vacancy during the diffusion process.

DFT is employed in order to compute the bulk properties in pure iron and a full set of SVI energies and migration barriers for the Fe(Cr), Fe(Cu), Fe(Mn), Fe(Ni), Fe(P) and Fe(Si) dilute binary alloys. The calculations were performed on a plane–wave basis, employing the pseudopotentials developed within the projector augmented wave (PAW) method [42, 43]. The exchange correlation function was described through the Perdew-Burke-Ernzerhof (PBE) parameterization [44] of the generalized gradient approximation (GGA). All calculations were spin polarized and the Vosko–Wilk–Nusair (VWN) algorithm [45] was used for the spin interpolation of the correlation potential. The Brillouin zone was sampled with the Monkhorst–Pack scheme.

The simulations were carried out on a 128–atom bcc supercell with full periodic boundary conditions. A plane wave cutoff of 300 eV and a $3 \times 3 \times 3$ k–point mesh were chosen, in accordance with the convergence tests of a previous study [46]. The defects were introduced allowing for atomic relaxations but restraining the cell shape and volume. In pure iron, the vacancy formation enthalpy is computed as $E_v^{\mathrm{form}} = E(N-1) - (N-1)/N \cdot E(N)$, where $E(N)$ is the energy of the undefected supercell and $E(N-1)$ that of the system containing a vacant site. The further introduction of a solute atom yields the solute–vacancy binding energy (at the X-nn distance):

$$E^b_{V,X\mathrm{nn}} = E^{N-2}_{1V,\,1\mathrm{sol}\,(X\mathrm{nn})} - E^{N-1}_{1V} - E^{N-1}_{1\mathrm{sol}} + E^N \ , \quad (3)$$

where the terms on the right-hand side are the energies of the supercell respectively with one substitutional solute atom and one vacancy, with only one vacancy, with only one solute atom and without any defect.

The nudged elastic band (NEB) method [47, 48], implemented with 3 images and the climbing–image algorithm [49], was employed for the evaluation of the system energy at the saddle point for all jump configurations. In the climbing–image algorithm, 3 images are sufficient for an accurate evaluation of the saddle point energy [50], since all barriers here investigated are of single hump shape. The migration barriers are defined as energy difference between the saddle point and the initial state. Each NEB simulation yields the migration energy of a forward jump ($E^{\mathrm{mig}}_{ij} = E^{ij}_{\mathrm{sad}} - E^{i}_{\mathrm{relax}}$) and its backward counterpart ($E^{\mathrm{mig}}_{ji} = E^{ij}_{\mathrm{sad}} - E^{j}_{\mathrm{relax}}$). The uncertainty related to the computed binding energies and migration barriers is estimated to about 5 meV.

The standard potentials available in the VASP library were employed for all involved chemical elements. Concerning the calculations in the Fe(Mn) alloy, it was previously reported that some NEB simulations did not converge to a physically meaningful magnetic state [37] and led to anomalously high migration barriers (> 1 eV) [51]. A similar issue was encountered in the Fe(Si) alloy. Once more, the system was successfully driven to the correct global minimum with the use of linear mixing in the starting guess of the charge dielectric function, as opposed to using the Kerker model [52, 53].

The jump frequency prefactor ν_i^* might also be computed ab initio, by means of frozen phonon calculations and the application of Vineyard's theory [36]. The same calculations allow as well for the computation of the vacancy formation entropy [54]. However, this is beyond the scope of this work since the drag tendencies are weakly affected by the attempt frequency value [55], as long as the latter is the same for all jump types. Hence, the attempt frequency is assumed to be the same for all kind of jumps and of the same order of magnitude of the Debye frequency in iron: 6 THz [56].

Ab initio results

The bulk properties of pure iron are reported in Table I. The computed equilibrium lattice parameter is consistent with previous VASP calculations [35, 57]. The total vacancy diffusion activation energy in pure iron of 2.88 eV is in line with previous DFT calculations [58, 59] and close to the experimental value of 2.95 eV [60]. The vacancy formation entropy was computed with DFT by Lucas et al. [61]. Their larger value of $4.1 k_B$ with respect to previous calculations [62, 63] is anyway consistent with the total value for formation and migration entropy of $5 k_{\mathrm{B}}$ found in another study [64]. However, the entropy of migration is neglected in this work.

The binding energies obtained by supercell relaxation with the VASP code are reported in Fig. 2. The solutes are ordered from the strongest binding (P) to the weakest (Cr). It is evident that all solutes, with the exception of Cr, present a strong binding character with vacancies, which confirms the findings of previous DFT calculations [35]. As already argued in the same reference, the binding character for the transition metals in the 3d group is most likely caused by a strong magnetic coupling. For the oversized impurities (Cu, Mn, Ni) the strong interaction arises also because of strain relief in the matrix.

The general agreement with previous computations and experimental data is quite satisfactory. A minor dif-

TABLE I. Bulk properties (computed or adopted in this work), compared with experiments and previous calculations.

Quantity	This work	Previous calculations	Experiments
Lattice parameter a_0	2.831 Å	2.83 Å[a] , 2.86 Å[b]	2.86 Å[k]
Vacancy formation enthalpy H_v^{f}	2.18 eV	2.20 eV[c], 2.02 eV[d], 2.16 eV[e]	1.60 eV[l], 2.0 eV[m]
Vacancy migration energy E_v^{mig}	0.70 eV	0.67 eV[c], 0.65 eV[d]	0.55 eV[n]
Ferromagnetic activation energy Q_v^F	2.88 eV	2.87 eV[c], 2.67 eV[d]	2.95 eV[o], 2.88 eV[l]
Vacancy formation entropy S_v^f	$4.1 k_{\mathrm{B}}$[e]	1.5-2.0k_{B}[f], $2.1 k_{\mathrm{B}}$[g], $< 5\, k_{\mathrm{B}}$[h]	
Attempt frequency ν_0^*	6 THz	91.5 THz[i], 4.9 THz[j]	

[a] Reference [35]. [b] Reference [57]. [c] Reference [59]. [d] Reference [58]. [e] Reference [61]. [f] Reference [63]. [g] Reference [62]. [h] Reference [64]. [i] Reference [67]. [j] Reference [19]. [k] Reference [56]. [l] Reference [65]. [m] Reference [66]. [n] Reference [68]. [o] Reference [60].

ference is related to Cu, for which previous computations performed with the Ultra Soft Pseudo-Potential (USPP) yielded a stronger interaction at 2nn than 1nn. Concerning the experimental measurements, the 1nn and 2nn can not be distinguished in bcc crystals, due to their similar relative distance. Furthermore, the Cr experimental value that is shown in Fig. 2 represents the upper bound of the interaction energy [69] and is therefore in agreement with this work's calculations.

The interaction is strong up to the 2nn distance, beyond which it abruptly drops to zero. This is due to the relatively short distance between second nearest neighbors in bcc crystals, with respect, for instance, to that in the fcc structure. The anomalous behavior shown by Ni, namely the stronger 2nn interaction, was also observed for cobalt [35]. The reason is to be investigated by a more in-depth analysis of the magnetic coupling that is beyond the scope of this paper. In general, the binding character of the solute–vacancy interaction is a hint that dragging by vacancies is likely to occur, although it is not possible to state a priori its strength and temperature dependence.

In some cases (Cu, Mn, Ni) there exists a weak attraction between solute and vacancy at the 5nn distance. This residual interaction is caused by elastic interactions among the atoms lying on the close-packed ⟨111⟩ direction, as the next atom in line (10nn) is also characterized by a slightly higher binding energy than the 9nn or 11nn (not shown in the graph). In order to investigate the effect of this non-negligible interaction, the thermodynamic model for the computation of the transport coefficients was therefore extended to the 5nn. Models neglecting the 2nn interaction are likely to yield unreliable results, given the strong 2nn interaction in most of the studied alloys.

The following step is the calculation of the migration barriers for the network of 12+2 jump frequencies (for each impurity) described in Fig. 1. Table II shows the energy barriers obtained via NEB calculations. They are also compared to previous computations performed with different DFT parameters [19, 22, 50, 51] and with DFT calculations performed with the SIESTA code [59]. In addition, the same migration barriers are represented in

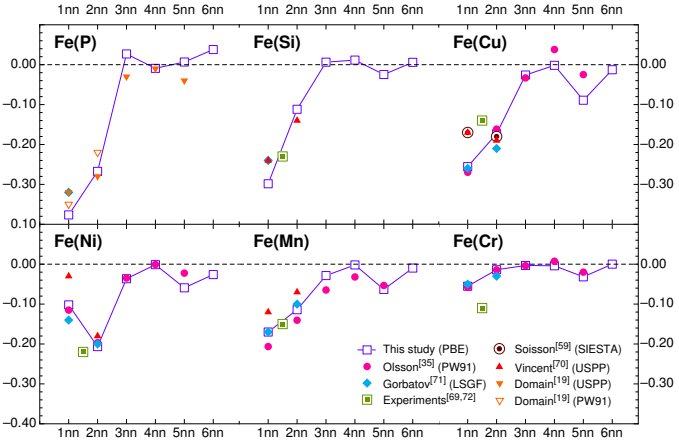

FIG. 2. Ab initio solute–vacancy binding energies (in eV) obtained by supercell relaxation, compared with previous calculations [19, 35, 59, 70, 71] and experiments [69, 72]. Negative energies stand for attractive interactions.

Fig. 3 as function of the solute-vacancy distance. As expected, the migration barriers approach the background value ω_0 as the solute–vacancy distance increases, since the interaction fades out with distance.

Generally speaking, the attractive binding energy leads to an increment of the dissociative migration barriers and to a decrement of the associative counterparts. The effect is more prominent when the binding energy is stronger (P, Si), whereas all values are close to ω_0 in the Cr case. A higher solute-vacancy association rate than dissociation means in physical terms that the probability for a vacancy to abandon the interaction area around the solute is small. Nevertheless, at least another ω_{ij} frequency is necessary for the vacancy to turn around the solute and yield a net displacement, as observed in the AB model alloy [31]. Therefore, the calculation of transport coefficients is unavoidable if one is to investigate the possibility of vacancy drag.

In most cases, the agreement with previous calculations is good. The only remarkable exception is represented by the ω_2 frequency for Mn. The much higher value of 1.03 eV previously reported by Vincent et al.

[51] and applied to their KMC model was affected by the problematic convergence of the Mn magnetic state, as the same authors mentioned. It can be observed that all here-studied impurities are characterized by a higher migration frequency, if one assumes the attempt frequency ν_2^* to be comparable to ν_0^*. In this regards, the result of Ni is in partial contradiction with the findings of Choudhury et al. [22], who observed a higher solute migration barrier than that of pure iron. This inconsistency can be related to their smaller supercell size (54 atoms). It is worth noticing that a higher solute–vacancy exchange frequency does not necessarily entail a faster impurity diffusion, as the $D_{\mathrm{sol}}/D_{\mathrm{Fe}}$ ratio depends on the drag tendency as well.

COMPUTATION OF THE TRANSPORT COEFFICIENTS

Manipulation of jump frequencies

For practical reasons, the long–ranged SVI must be cut off at a finite distance in order to limit the amount of equations of the analytical mean field model. In a dilute alloy, this entails the distinction between an interacting area around the solute atom and the background. The former is represented by the ensemble of atoms located at a distance from the solute within the chosen interaction range. The solute-vacancy pair is regarded as associated (i.e. there exists a non-null SVI) when the vacancy is inside the interaction area, or dissociated otherwise.

Once the cutoff is introduced, the binding energy beyond this distance must be set to null ($E^b_\infty = 0$). This implies a manipulation of the DFT–computed jump frequencies, in order to respect the detailed balance requirements [73]. According to the detailed balance principle, each elementary transition must be balanced by its reverse process in thermodynamic equilibrium conditions. In general, this means that the forward and backward transitions between two states i and j occur at the same rate:

$$\omega_{ij}^{(0)} p_i^{(0)} = \omega_{ji}^{(0)} p_j^{(0)} \quad , \tag{4}$$

where the probability p of each state depends upon the energy of the state through the classic Boltzmann factor $\exp\left(-\mathrm{E}/\mathrm{k_B T}\right)$. In the specific case of atom–vacancy exchange, all couples of forward–backward jumps (ω_{ij}, ω_{ji}) are bound to this condition. Since the energy of the initial and final configurations can be expressed in terms of binding energy difference:

$$\frac{\omega_{ij}}{\omega_{ji}} = \exp\left(-\frac{E_j^b - E_i^b}{k_B T}\right) \quad , \tag{5}$$

it follows that $E_i^b - E_j^b = E_j^{\mathrm{mig}} - E_i^{\mathrm{mig}}$, if the attempt frequencies are assumed to be the same for all jumps.

The practical consequence on the set of DFT–computed migration barriers is that any sequence of jumps starting from the same i–nn position and leading to a dissociation must occur at the same rate:

$$\frac{\omega_{\infty i}}{\omega_{i\infty}} = \frac{\omega_{\infty j}}{\omega_{j\infty}} . \frac{\omega_{ji}}{\omega_{ij}} = \frac{\omega_{\infty l}}{\omega_{l\infty}} . \frac{\omega_{lk}}{\omega_{kl}} . \frac{\omega_{ki}}{\omega_{ik}} = \dots \ (\ i,\, j,\, k,\, l \leq \hat{R}) \ , \tag{6}$$

where the jump chain can consist of several jumps ($i \to \infty$, $i \to j \to \infty$, $i \to k \to l \to \infty$, and so on). The ∞ symbol marks any nn distance beyond the interaction zone.

The set of DFT migration barriers is therefore modified in order to comply to the requirement of null binding energy beyond $\hat{R}$. The most straight–forward way is to keep the ab-initio computed saddle point energy constant and let the associative frequencies of type $\omega_{\infty i}$ ($i \leq \hat{R}$) change, so that $E^{\mathrm{mig}}_{\infty i}$ is decreased exactly by the binding energy that is to be neglected. For instance, setting $E_3^b = 0$ makes the activation energy of the jump ω_{31} decrease by the DFT value of E_3^b. It is clear that this approach has little effect on the interaction physics as long as the binding energies to be neglected are small. Given the non–negligible values of E_5^b, cutting the thermodynamic range to the 2nn would lead to a considerable modification of the backward frequencies. For this reason, the cutoff range was set on the 5nn distance, resulting in the jump frequency network shown in Fig. 1.

Several range cutoffs were explored, leading to three distinct frequency sets, whose performances are compared in terms of drag predictability.

A) 5nn set: all DFT jump frequencies are introduced. The backward frequencies are modified according to the procedure described above, so that the binding energies beyond the 5nn are null.

B) 2nn set: only frequencies related to the 1nn and 2nn are considered (ω_{12}, ω_{13}, ω_{15}, ω_{24}). The backward frequencies are modified in the same fashion in order to set the binding energies beyond 2nn to zero. By comparing the 2nn set to the 5nn set, the influence of E_5^b in terms of vacancy drag can be determined. This model represents a considerable advancement with respect to the most advanced existing 2nn models [25, 26], as the latter assume the backward jumps ω_{31}, ω_{51} and ω_{42} to occur at the background frequency ω_0. As a consequence, the associative tendency of the vacancy-solute pair is seriously underestimated.

C) 1nn set: the thermodynamic SVI is truncated to the first nn sites. The frequencies involved are ω_{12}, ω_{13} and ω_{15}. In this case, a unique $\omega_{1\infty}$ frequency is calculated as $7\omega_{1\infty} = 3\omega_{12} + 3\omega_{13} + \omega_{15}$ (and analogously for $\omega_{\infty 1}$). Many analytical models available in the literature (for instance, the 4–frequency model in [24]) are limited to the 1nn; it is therefore

TABLE II. Ab–initio migration barriers (in eV) computed in this study and comparison with previous DFT calculations (in square brackets), according to the jump frequency nomenclature described in Fig. 1.

	P		Si		Cu		Ni		Mn		Cr	
ω_0	0.70 [0.67]^a, [0.68]^e, [0.65]^f											
ω_2	0.40 [0.34]^d, [0.31]^g		0.51 [0.44]^c		0.51 [0.59]^e, [0.56]^c		0.63 [0.68]^a, [0.70]^c		0.42 [1.03]^c		0.53 [0.58]^a, [0.62]^b	
ω_{12}, ω_{21}	0.68 [0.60]^d	0.57 [0.56]^d	0.74 [0.65]^c	0.55	0.72 [0.64]^e [0.60]^c	0.64 [0.64]^e	0.59 [0.55]^a [0.46]^c	0.69 [0.69]^a	0.66 [0.64]^c	0.61	0.69 [0.69]^a [0.69]^b	0.66 [0.65]^a [0.64]^b
ω_{13}, ω_{31}	0.98 [0.92]^d	0.58 [0.59]^d	0.89 [0.84]^c	0.58	0.74 [0.70]^e [0.67]^c	0.51 [0.56]^e	0.72 [0.70]^a [0.69]^c	0.66 [0.67]^a	0.70 [0.66]^c	0.55	0.69 [0.67]^a [0.69]^b	0.64 [0.63]^a [0.63]^b
ω_{15}, ω_{51}	0.86 [0.68]^d	0.47 [0.34]^d	0.82 [0.65]^c	0.55	0.67 [0.63]^e [0.62]^c	0.50 [0.53]^e	0.66 [0.62]^a [0.63]^c	0.62 [0.59]^a	0.66 [0.62]^c	0.55	0.67 [0.64]^a [0.67]^b	0.65 [0.62]^a [0.64]^b
ω_{24}, ω_{42}	0.74 [0.68]^d	0.48 [0.37]^d	0.71	0.58	0.75 [0.74]^e	0.57 [0.55]^e	0.80	0.59	0.76	0.64	0.72	0.70
ω_{34}, ω_{43}	0.66	0.69	0.68	0.67	0.69	0.67	0.70	0.67	0.68	0.66	0.68	0.68
ω_{37}, ω_{73}	0.69	0.70	0.69	0.69	0.69	0.68	0.70	0.68	0.69	0.69	0.69	0.70
ω_{45}, ω_{54}	0.66	0.65	0.67	0.70	0.68	0.77	0.69	0.75	0.69	0.75	0.68	0.71
ω_{46}, ω_{64}	0.68	0.63	0.65	0.66	0.67	0.68	0.68	0.70	0.68	0.69	0.70	0.70
ω_{48}, ω_{84}	0.69	0.67	0.69	0.69	0.70	0.70	0.70	0.70	0.71	0.70	0.71	0.70
ω_{49}, ω_{94}	0.69	0.71	0.69	0.72	0.70	0.70	0.70	0.70	0.70	0.69	0.70	0.70
ω_{57}, ω_{75}	0.69	0.68	0.68	0.65	0.71	0.63	0.70	0.66	0.70	0.65	0.69	0.67
$\omega_{5\,10}, \omega_{10\,5}$	0.67	0.66	0.68	0.65	0.70	0.64	0.71	0.68	0.70	0.67	0.70	0.69

[a] Reference [22], PAW–PBE.
[b] Reference [50], PAW–PBE.
[c] Reference [51], PAW–PW91.
[d] Reference [19], USPP.
[e] Reference [59], SIESTA.
[f] Reference [58], PAW–PW91.
[g] Reference [16], interatomic potential.

interesting to analyze the accuracy of such a simple model in terms of solute diffusion by vacancies.

In addition to the 1nn, 2nn and 5nn sets, a further set was derived from the DFT database by using the Final Initial State Energy (FISE) approximation. FISE is an alternative model that is very often employed to predict migration barriers, when DFT calculations are not available for all atomic configurations. It was used in the past under different names [31, 74, 75], as it is the most commonly employed model in atomistic kinetic Monte Carlo (AKMC) simulations.

The amount of migration barriers computed in this work makes possible to assess the reliability of the FISE approach and the consequences in terms of vacancy–drag predictability. In this model, the migration barrier E_{ij}^{mig} between configurations i and j depends on a reference migration barrier and the energy difference between the final and initial state:

$$E_{ij}^{\mathrm{mig}} = E_0^{\mathrm{mig}} + \frac{E_j - E_i}{2} \, . \qquad (7)$$

E_0^{mig} usually depends on the jumping species: ω_0 for the host atom and ω_2 for the solute. The model always ensures fulfillment of the detailed balance condition. The energy of the end states can be computed through ab initio relaxations (this work) or many available broken bond models, whereas the reference migration barrier E_0^{mig} can be obtained through several methods (for an extensive review of such methods, see [76]). More advanced models allow to take into account the local chemical environment around the jumping atom at the saddle point (see for instance [50]) in the case of concentrated alloys.

The main issue related to the use of this simple model is that in reality the energy of the arriving state is not known a priori. In order to assess its reliability in terms of jump frequency prediction and diffusion modeling, a set of jump frequencies is computed based on the DFT initial and final state energies obtained in this work. E_0^{mig} is given by the unperturbed Fe-V migration barrier (0.70 eV). Applying Eq. 7 entails that all forward-backward migration barriers are shifted so that they are symmetric with respect to ω_0.

The four sets of jump frequencies are shown in Fig. 3 for each impurity. It is made a distinction between forward (full symbols) and backward (blank symbols) jumps, in order to emphasize the lower probability for dissociation jumps. It can be observed that the FISE migration barriers based on DFT–computed end–state energies are in most cases in disagreement with the NEB values inside the interaction shell, whereas they agree quite well beyond the ω_{24} jump type.

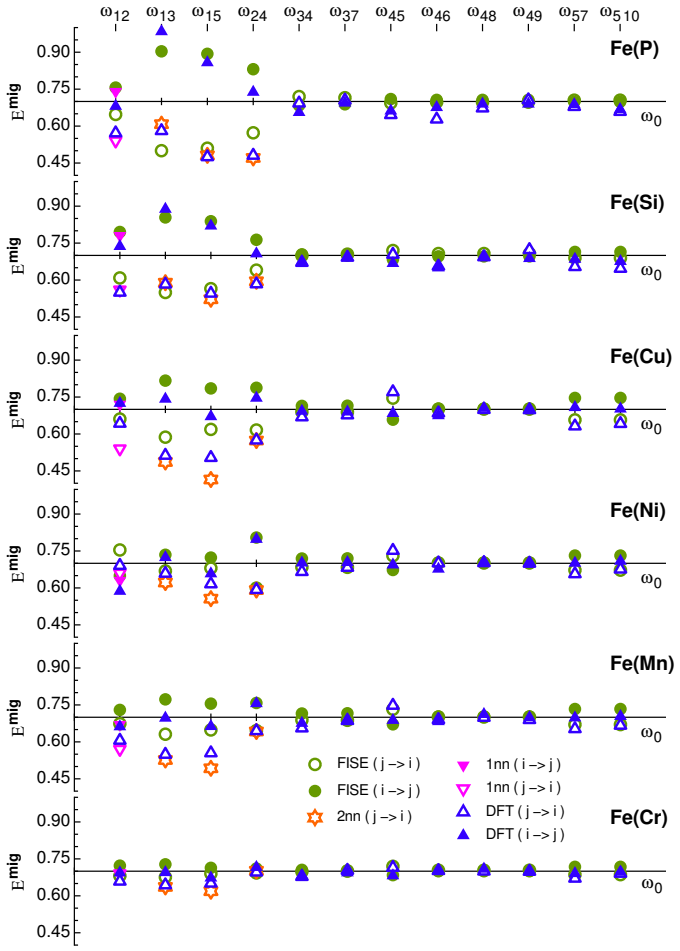

FIG. 3. Migration barriers (in eV) for Fe-V jumps of type ω_{ij}, where i is the initial nn position of the vacancy with respect to the solute, and j the distance after the jump. Backward jumps (from configuration j to i) are shown with blank symbols. DFT-calculated values are compared to those obtained with the Final Initial State Energy (FISE) approach. The modified barriers for the 1nn and 2nn sets are also shown.

Finite–temperature magnetic model

In order to allow for a comparison with diffusion experiments, which are usually performed at relatively high temperatures, magnetic disordering must be taken into account. It is here assumed that the magnetic transition to the paramagnetic state leads to a progressive reduction of the self–diffusion activation energy $Q_0^F = E_v^{\rm form} + E_v^{\rm mig}$. The reduction is proportional to the magnetic excess enthalpy $\mathrm{H}^{\rm mag}$ [77]:

$$Q(T) = Q_0^F - \alpha H(T)\ . \qquad (8)$$

The normalized coefficient $H(T)=1-H^{\rm mag}(T)/H^{\rm mag}(0)$ is defined so that H=0 at 0 K and H=1 in a perfectly disordered state. The model yielding the excess enthalpy $H^{\rm mag}$ is described in [78]. Short range ordering is represented as residual magnetization above the Curie temperature. From this definition it follows that $\alpha = Q_0^F - Q_0^P$, where Q_0^P is the activation energy in fully paramagnetic state. Such a value can be inferred from experiments or computed with first-principle methods. In this work, $Q_0^P = 2.26$ eV is taken from the ab initio calculations by Chang et al. [77]. It is worth noticing that this magnetic effect appears as the same multiplicative factor in all Onsager coefficients. It therefore does not affect the drag coefficient given by the ratio L_{BV}/L_{BB}. Although this magnetic model was devised only for self-diffusion in pure iron and fitted to self–diffusion experiments, it is assumed that the presence of one solute atom has a negligible effect on the magnetic transition.

SCMF model

The sets of jump frequencies are used as input parameters for the calculation of the transport coefficients, in the framework of the Self Consistent Mean Field (SCMF) theory. The interested reader can find in [27, 28, 31] further details about the SCMF model and its solution.

One of the main features of the SCMF method is the distinction between thermodynamic and kinetic interatomic interactions. The former determine the probability of a certain crystal configuration to occur in thermodynamic equilibrium conditions, and correspond to the binding energies shown in Fig. 2. As already discussed, a range cutoff has to be imposed in practice and is differently chosen in the aforementioned frequency sets.

The kinetic interactions are fictitious interactions that are introduced in the Hamiltonian of the system in order to describe the probability perturbation of a certain configuration in near–equilibrium conditions. At equilibrium they are null by definition. The amount of introduced interactions depends on a cutoff range that is analogous to the previous cutoff, but is now referred to the kinetic interactions. The kinetic interaction shell has to necessarily include the thermodynamic shell in order to properly describe the system thermodynamically.

The choice of the kinetic shell is strictly related to the vacancy migration paths. The migration paths that are outside the kinetic interaction shell are in facts not considered in the mean field model. On the other hand, the ability of a vacancy to drag a solute atom depends on its possibility to turn around the solute between two consecutive solute–vacancy exchanges. The vacancy may follow different paths. It was shown in [31] that, in bcc crystals, paths beyond the 1nn and 2nn position are also important for such phenomenon (for instance the 2nn-4nn-3nn-4nn path). It is therefore evident that any kinetic model being limited to the 1nn or 2nn would miss out some of the possible drag patterns.

In that work the extent of the interaction shell reached the 3nn of 3nn sites (referred to as the 3nn3nn model). Since in this work the thermodynamic interactions are

cut off at the 5nn distance, the kinetic model is extended to the 5nn(1nn)^k sites. The truncation at the k:th shell implies that the calculation is exact for sequences of maximum k jumps [31]. In another work [32] it was shown that in the case of a 3nn(1nn)^k approximation in fcc crystals the error decreases exponentially with k. The result is confirmed in this work for the 5nn(1nn)^k approximation in bcc crystals by performing convergence tests. A truncation to k=2 leads to a relative error of less than 0.01% in the computation of the L_{AB} coefficient (which is the most sensitive one) with respect to k=3. For this reason, the approximation adopted in this work for the 5nn frequency sets is 5nn(1nn)^2, hence 1nn of 1nn of (1nn, 2nn, 3nn, 4nn, 5nn). Conversely, the kinetic models for the 2nn and 1nn frequency sets are respectively 3nn3nn and 1nn1nn, for the sake of consistency with the thermodynamic assumptions.

As a benchmark for the obtained transport coefficients, AKMC simulations were performed, limitedly to a 2nn(1nn)^k kinetic model, by using the LAKIMOCA code [57]. In the AKMC framework, the phenomenological coefficients are obtained with the Kubo–Green formula [23]:

$$L_{ij} = \frac{\Delta\vec{R}_i \cdot \Delta\vec{R}_j}{6Vt} \ , \tag{9}$$

where $\Delta\vec{R}_i$ is the total displacement of all atoms of species i in time t and V is the system volume. With such a definition, the Onsager coefficients are expressed in (ms)$^{-1}$ units.

The simulation box contains 432 sites disposed in a $6 \times 6 \times 6$ bcc cell, with one solute atom and one vacancy. As a single solute atom is present in the box, no solute-solute interaction takes place and the dilute limit behavior is simulated even though the nominal concentration of 0.23% might seem not representative of a dilute alloy. Convergence is reached after $3 \cdot 10^{10}$ atomic jumps and the atomic paths are sampled every 5000 steps, hence after approximately 10 jumps in average for each atom.

Applications of the Onsager matrix

An accurate computation of the Onsager matrix enables to investigate several different properties of the system that rely on the coupling between different diffusion fluxes. In this work, the Lij:s are employed for the determination of the vacancy drag factor L_{BV}/L_{BB}, the solute tracer diffusion coefficients D^*_B and the RIS tendency.

In a dilute binary alloy, a solute atom can diffuse in the opposite direction than that of vacancies (inverse Kirkendall), or in the same direction (vacancy drag). Solute drag by vacancies is a common phenomenon that can occur, under certain conditions, in several types of alloy [31]. Contrary to a common misconception, the conventional thermodynamic SVI is not the only ingredient determining the possibility of vacancy drag. For instance, it is shown in [31] that in alloys with no thermodynamic interactions, drag can still occur if the set of jump frequencies in the interaction zone allows the vacancy to complete a path around the solute. It depends in facts in a intricate manner on the several jump frequencies involved inside and across the interaction zone. For such a reason, a prediction of solute drag exclusively based on interaction energies is likely to fail.

In this work, solute drag was investigated following the approach of Anthony [79], i.e. by calculating the ratio L_{BV}/L_{BB}, where $L_{BV} = -(L_{AB} + L_{BB})$. In this framework, the ratio is positive when drag occurs, or negative otherwise.

Given the impossibility of measuring the full Onsager matrix by experiments, a way to benchmark the model is to compare with measured solute tracer diffusion coefficients D^*_B, which can be directly derived from the L_{BB} coefficient. In a dilute alloy, the solute tracer and intrinsic diffusion coefficients coincide. Hence, a unique diffusion coefficient can be defined [73]:

$$D^*_B = D_B = \frac{L_{BB}}{nC_B} \ , \tag{10}$$

where n is the number of atoms per atomic volume and C_B the solute concentration.

The coefficients of the Onsager matrix can also be used to derive RIS tendencies in multicomponent alloys. In the particular case of dilute alloys, RIS phenomena in dilute alloys are easier to describe thanks to the reduced amount of jump frequencies involved and the clear definition of the solute–vacancy interaction. Consequently, the derivation of the Lij coefficients through the SCMF method guarantees a high degree of accuracy in the RIS prediction.

A continuous model relying on the knowledge of the Onsager coefficients [4, 80] is here applied. When defect and chemical fluxes are in dynamic equilibrium, the following relationship between chemical and defect concentration gradients near defect sinks can be derived:

$$\frac{\nabla C_B}{\nabla C_V} = \frac{C_A C_B d_{AV} d_{AI}}{(C_A d_{AI} D_B + C_B d_{BI} D_A)} \left(\frac{d_{BV}}{d_{AV}} - \frac{d_{BI}}{d_{AI}} \right) \ , \tag{11}$$

where C_i represents the equilibrium concentration of species (or defect) i, D_i the intrinsic diffusion coefficient and d_i the partial diffusion coefficients that depend on the L_{ij}:

$$d_{AV} = \frac{L^V_{AA} + L^V_{AB}}{C_A C_V} \ , \ d_{BV} = \frac{L^V_{AB} + L^V_{BB}}{C_B C_V} \ . \tag{12}$$

Similar partial diffusion coefficients are defined for interstitial mediated diffusion (a detailed description of the terms in Eq. 11 can be found in [4], and a misprint

in the same equation has been corrected here). Since the present work is limited to vacancy diffusion, a precise evaluation of the ratio $\Delta C_B/\Delta C_V$ is not achievable. However, the RIS trends solely due to vacancies can be qualitatively inferred by the ratio d_{BV}/d_{AV}, as long as the analogous ratio d_{BI}/d_{AI} is set equal to 1.

As far as vacancy diffusion is concerned, there exists a clear correlation between diffusion mechanism and RIS tendency. If vacancy drag occurs, d_{BV} is negative (while d_{AV} is always positive): only solute enrichment at PD sinks is possible, as the solute atoms follow the vacancies migrating towards the sinks. In the case of inverse Kirkendall mechanism, the partial diffusion coefficient ratio is always positive, but enrichment of B can still occur if $d_{BV} < d_{AV}$, i.e. if the solute moves slower than the matrix atoms. In this specific case, the L_{AB} coefficient can be negative but is always greater than -1. Finally, solute depletion at sinks occurs when $d_{BV} > d_{AV}$.

Dilute limit and vacancy concentration

The transport coefficients are derived in the dilute limit ($C_B \to 0$). $L_{AB} = l_{AB} \cdot C_B$ and $L_{BB} = l_{BB} \cdot C_B$ are directly proportional to C_B, as second- and higher-order terms in C_B are neglected. Concerning the L_{AA} coefficient, there is also a zero order term: $L_{AA} = L^0_{AA} - l_{AA} \cdot C_B$ (where l_{AA} expresses the effect of the A–B correlation). Therefore in the dilute limit, the drag factor L_{BV}/L_{BB}, the solute tracer coefficient D^*_B and the partial coefficient d_{BV} are independent from the solute concentration. As well, a first order expansion of d_{BV} implies that the ratio d_{BV}/d_{AV} is properly defined at zero order only: $d_{BV}/d_{AV} = (l_{AB} + l_{BB})/L^0_{AA}$.

The vacancy concentration is assumed to be that of the thermodynamic equilibrium (i.e. non–irradiated) conditions:

$$C_V^{eq} = \exp\left(-\frac{H_v^f}{k_B T}\right) \cdot \exp\left(\frac{S_v^f}{k_B}\right) \qquad (13)$$

The effect of irradiation would be to increase the number of vacancies of the system, and increase at the same extent the transport coefficients, which are proportional to C_V. The drag and RIS tendencies given by the partial diffusion coefficient ratio would not change (although the RIS effect would increase in magnitude). As for the comparison to experimental diffusion coefficients, they are always performed in non-irradiated conditions.

Results and discussion

Onsager coefficients and vacancy drag

The obtained Onsager coefficients are shown in Fig. 4 (exclusively for the 5nn model), where the solute concentration C_B is assumed to be 1% and the equilibrium vacancy concentration is given by Eq. 13. The magnetic correction is not applied. It is worth observing that the L_{AB} coefficient deviates from the Arrhenius behavior because of the strong correlations between vacancy and solute flux. Therefore, extrapolation from the high–temperature regime to the low–temperature one would lead to an error estimable up to two orders of magnitude.

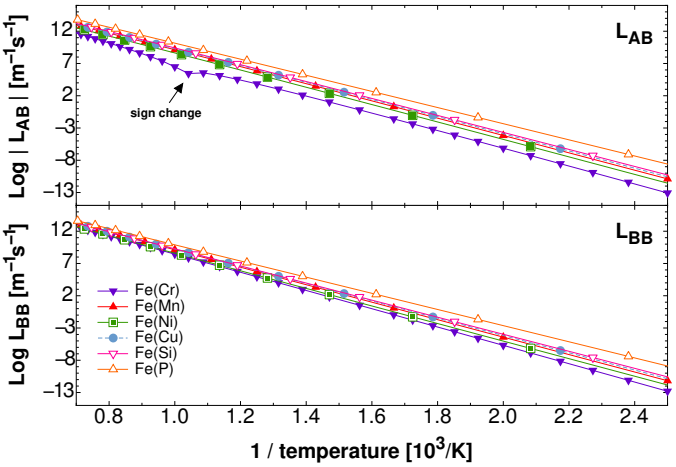

FIG. 4. Off-diagonal (L_{AB}) and solute (L_{BB}) Onsager coefficients, obtained with the SCMF method in the 5nn model for each binary alloy and a solute concentration of 1%. L_{AB} is negative for all solutes except Cr, in which case $L_{AB} > 0$ for $T > 970$ K.

In the dilute limit ($C_B \to 0$), L_{AA} approaches L^0_{AA} and is independent from the solute species, as it represents the uncorrelated part of the Fe-Fe transport coefficient. L^0_{AA} (not shown in Fig. 4) is characterized by a perfect Arrhenius temperature dependence, where the prefactor is $2.6 \cdot 10^{24}$ $(\text{ms})^{-1}$ and the slope is $Q = 1.25$ eV. L_{BB} is always positive as it should be according to the second law of thermodynamics, and is directly related to the solute diffusion coefficient. L_{AB} determines the sign of the wind factor, hence the dragging behavior. It can be observed that in all cases except Cr the L_{AB} coefficients are negative. This does not necessarily entails solute drag: if $L_{AB} > -1$, species A and B move in the same direction under a gradient of vacancy chemical potential.

The magnitude of the L_{AB} coefficient is larger in the systems where the SVI are stronger. Only when the critical condition $L_{AB} = -L_{BB}$ (or equivalently $L_{BV} = 0$) is reached, solute drag arises. For this reason, the ratio L_{BV}/L_{BB} (wind factor) is shown in Fig. 5 as function of temperature. In this plot the different sets of frequencies are shown, as well as the Lakimoca results and previous calculations of the wind factor for the Fe(Cr) [22], Fe(Ni) [22] and Fe(Cu) [20, 81] alloys.

There exists a minor difference between the 2nn and 5nn models, which implies that in these alloys it is com-

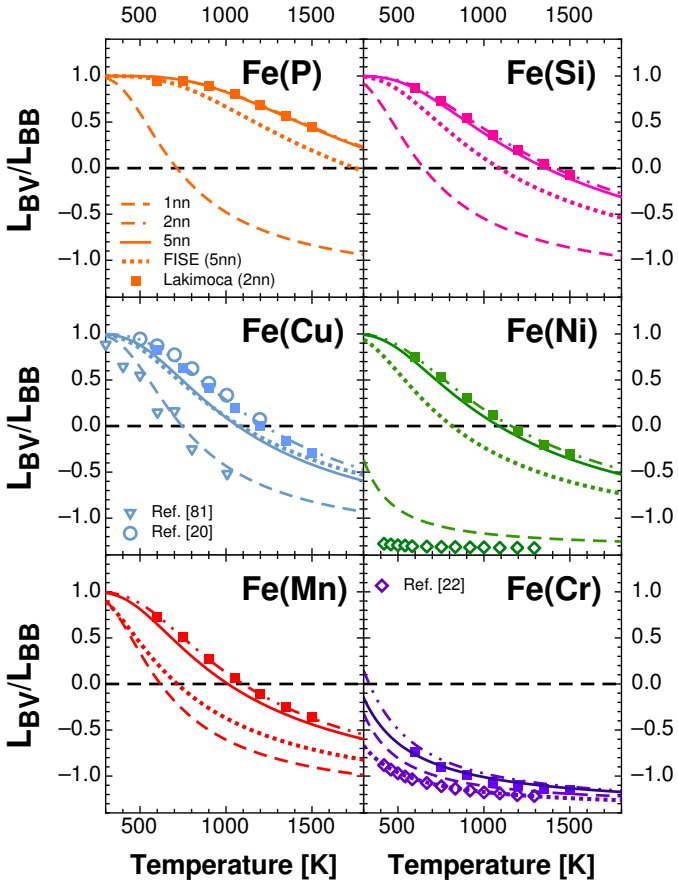

FIG. 5. Solute drag factors $L_{BV}/L_{BB} = -(1+L_{AB}/L_{BB})$ obtained with the SCMF method (lines) and with Monte Carlo simulations (dots) for each binary alloy, with several jump frequency sets (1nn, 2nn, 5nn and FISE). Drag occurs for values greater than 0. The 2nn-model curve overlaps with the 5nn-model one for Fe(P). Results of previous works are also shown for Fe(Cr) [22], Fe(Ni) [22] and Fe(Cu) [20, 81].

pletely acceptable to limit the interaction shell to the 2nn, even with the modifications to the backward frequencies imposed by the detailed balance condition. The largest discrepancy is in the Fe(Cu) system, where the strongest 5nn interaction is present: $\Delta(L_{BV}/L_{BB}) < 0.2$. Furthermore, the results of the 2nn model are perfectly reproduced by the KMC simulations, which confirms the reliability of the SCMF method. In the case of Fe(Cu), vacancy drag was already predicted by a KMC study based on ab-initio migration barriers [20], and the results match perfectly with the 2nn model of this study. It is worthwhile noticing that the available 2nn multifrequency models before SCMF [25, 26] are not suitable for flux coupling analysis because they underestimate the associative probability and yield wrong wind factors. This was clear in [37], where the application of such an approximated model was not conclusive for the Fe(Cu) and Fe(Mn) systems. It is also important to remember from [31] that the 3nn interaction gives a quite considerable contribution, so it should not be neglected a priori. Nevertheless, in this work the 3nn binding energy is always quite small; moreover, many of the transition metal impurities in iron do not have a strong 3nn interaction, therefore a complete 2nn model is suitable for solute drag prediction.

On the other hand, the 1nn model (dashed lines) is clearly unsuitable. The drag tendency is considerably underestimated, which marks the importance of the 2nn SVI in bcc crystals. The 1nn model is often used for modeling impurity diffusion because of its simplicity, but it evidently leads to wrong conclusions. For instance, in [22] it was deduced that no drag would occur in Fe(Ni). This conclusion is wrong because of the overly approximated model. Furthermore, solute drag in dilute Fe(Cu) was predicted in a Monte Carlo study based on a broken bond model developed for both Fe- and Cu-rich phases to simulate Cu precipitation, but the predicted drag tendency was weaker [81].

Finally, it can be observed that in most cases the drag tendency is surprisingly well reproduced by the set of frequencies calculated in the FISE approximation, in spite of the disagreement with the DFT-computed migration barriers inside the interaction shell. Exceptions are given by the Fe(Mn) and Fe(Cr) alloys, for which the FISE predictions are more inaccurate. At any rate, KMC simulations based on FISE seem to be suitable for modeling vacancy-solute behavior, provided that the cohesive model is reliable. FISE may therefore represent a good choice for calculations in multicomponent alloys, where the amount of jump frequencies to calculate is very large and cannot be computed in toto with ab initio methods.

In general, it stands out that vacancy drag is a common phenomenon occurring in all alloys and favored by low temperatures. This work shows that the conclusions of [31] for a general AB alloy apply also to the real dilute alloys here studied. A strong binding SVI (as for instance in FeP) has the effect of shifting the curve towards the low–temperature side. The limit for all curves at high temperatures corresponds to the case of an ideal alloy with no interactions; from Manning's theory [15], the theoretical L_{BV}/L_{VV} ratio is -1.388, which is approached at lower temperatures in the 1nn model. The SCMF theory in the 5nn(1nn)^2 kinetic model yields a value of -1.371, in slightly better agreement than the 3nn3nn model [31], since more paths around the solute atom are available for the vacancy.

There is a clear trend between binding SVI and drag, as visible in Table III. The solutes are ordered from the strongest binding (P) to the weakest (Cr). One can see in the 2nn and 5nn models that the critical temperature (under which drag occurs) decreases as the binding tendency becomes weaker. Longer-ranged interactions, even though not remarkably visible in Fig. 5, are in some cases unexpectedly important for the critical temperature. For instance, in Fe(Cu),where the E_5^b is the largest,

TABLE III. 1nn and 2nn binding energies ($E^b_{X\mathrm{nn}}$), transition temperature between drag and non-drag regime (T_{crit}) and wind factor at RPV operational temperature ($L_{BV}/L_{BB}(573\,\mathrm{K})$) for the different alloys. The solute atoms are ordered according to T_{crit} of the 2nn model.

	P	Si	Cu	Ni	Mn	Cr
Binding energies [eV]						
$E^b_{1\mathrm{nn}}$	−0.38	−0.30	−0.26	−0.10	−0.17	−0.06
$E^b_{2\mathrm{nn}}$	−0.27	−0.11	−0.17	−0.21	−0.11	−0.01
Model: 5nn						
T_{crit} [K]	$\approx 2100^a$	1360	1068	1087	1011	262
$L_{BV}/L_{BB}(573\,\mathrm{K})$	0.99	0.89	0.78	0.74	0.70	−0.74
Model: 2nn						
T_{crit} [K]	$\approx 2130^a$	1414	1223	1159	1099	333
$L_{BV}/L_{BB}(573\,\mathrm{K})$	0.99	0.91	0.88	0.79	0.78	−0.62
Model: 1nn						
T_{crit} [K]	714	650	744	$\approx 225^a$	619	$\approx 220^a$
$L_{BV}/L_{BB}(573\,\mathrm{K})$	0.38	0.19	0.44	−0.98	0.12	−0.89
Model: 5nn (with FISE approximation)						
T_{crit} [K]	1750	1090	1085	816	716	$\approx 10^a$
$L_{BV}/L_{BB}(573\,\mathrm{K})$	0.97	0.75	0.74	0.43	0.28	−1.02

[a] Linearly extrapolated data.

the drag tendency is weakened because of the higher frequency of the dissociative jump ω_{45} and T_{crit} is hence 15% lower. The wind factor at 573 K, which is approximately the operational temperature of RPV steels, follows the same trend. In every system, the 1-2 orbital is activated for solute drag and $|E^b_2| < |E^b_1|$. In this specific case, $|E^b_1|$ determines T_{crit} and the amplitude of the drag effect. Conversely, the Fe(Ni) system is exceptional, since $|E^b_2| > |E^b_1|$ and consequently T_{crit} and the wind factor are not determined by $|E^b_1|$ only. Evidently, the 2nn SVI is fundamental for a correct description of this alloy. On the other hand, in the 1nn model there is no clear relationship between binding tendency and critical temperature or wind factor, which clearly shows the unreliability of that model. As for the FISE–computed set of frequencies, the general trend is respected but the drag effect is slightly underestimated.

In conclusion, vacancy drag is an expectable phenomenon at RPV operational temperature. Even though vacancy mobility is rather small, radiation-enhanced and induced phenomena are likely to occur because of the strong drag tendency. Such tendency progressively fades out at temperatures that are close to the Curie temperature in pure iron (1043 K), therefore closer to the temperatures at which diffusion experiments are usually performed. At any rate, it is undoubtedly an important diffusion mechanism at RPV temperature, in competition with possible interstitial-mediated diffusion.

Diffusion coefficients and RIS

The comparison with experimental solute tracer diffusion coefficients allows for a validation of the model. As shown by Eq. 10, D_B is directly proportional to the L_{BB} coefficient. The latter is directly related to the solute-vacancy exchange frequency ω_2, however it is also affected by correlation effects. It can be observed in Fig. 4, for instance, that Si and Cu are characterized by a higher diffusion coefficient than Mn, although their migration barrier for the solute-vacancy exchange is considerably higher (0.51 eV versus 0.42 eV). Vacancy drag has therefore the effect of enhancing solute diffusion. It is also important mentioning that in the 1nn model the L_{BB} coefficient (and therefore the D_B coefficient) is strongly underestimated, which is consistent with the lack of drag predictive capability of this model. No substantial differences are observed between the 2nn and 5nn models.

The solute tracer diffusion coefficients D^*_B are shown in Fig. 6. In order to compare with experimental measurements, the effect of the magnetic transition is taken into account. It is worthwhile noticing that in non–irradiated diffusion experiments the interstitial concentration is always very low compared to that of vacancies. In spite of the arbitrariness introduced by the attempt frequency and vacancy formation entropy that were taken from previous calculations, the activation energies are in quite good agreement, especially at low temperatures (Ni, P), at which the magnetic correction is small. The magnetic transition seems also to be well reproduced for Si, Cu and Cr. The only remarkable disagreement is represented by the activation energy and magnetic transition of the D^*_{Mn} coefficient. The mismatch could depend on the complex magnetic behavior of Mn in Fe, which might not be well reproduced by the rudimental model here applied that was developed for pure iron.

Given the overall agreement between calculated and experimental values, it can be concluded that in the dilute limit the presence of a solute atom does not invalidate the bulk-iron magnetic model, except possibly the case of Fe(Mn). A more refined model, such as [38], would yield visible effects on the drag tendency and the diffusion coefficient slopes only in non-dilute alloys. It is also worth mentioning that the attempt frequency value in pure iron affects only the magnitude of the calculated diffusion coefficients. It would influence the drag tendency if it strongly depended on the relative distance between vacancy and solute atom, which is considered here to be unlikely. Even in this case, it was shown in [55] that the quantitative effect on T_{crit} would be limited.

The RIS tendencies can be discussed by looking at Fig. 7, where the partial diffusion coefficient ratio d_{BV}/d_{AV} is shown for all binary alloys in the 5nn model. Only the contribution from the vacancy mechanism is considered. The ratio of partial diffusion coefficients due to interstitial mechanism is set to 1 and the prefactor of Eq. 11 is assumed to be always positive.

With the exception of Cr, the solutes show a common trend. Vacancy drag obviously entails solute enrichment, as the vacancy concentration gradient is negative at sinks. Therefore, solute enrichment is expected

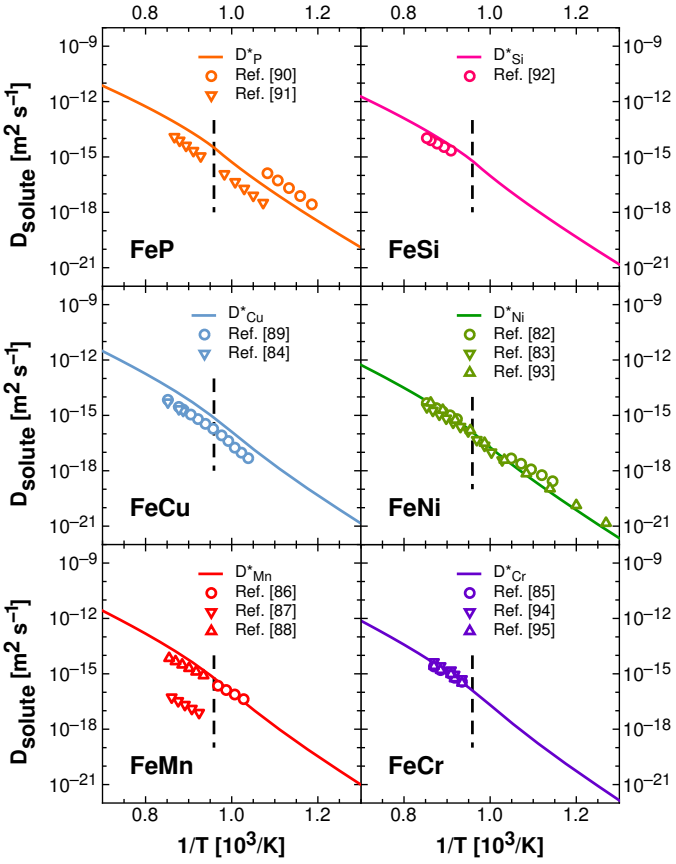

FIG. 6. Comparison of solute tracer diffusion coefficients computed with the SCMF method in the 5nn model with experiments [82–95]. The dashed line marks the magnetic order–disorder transition.

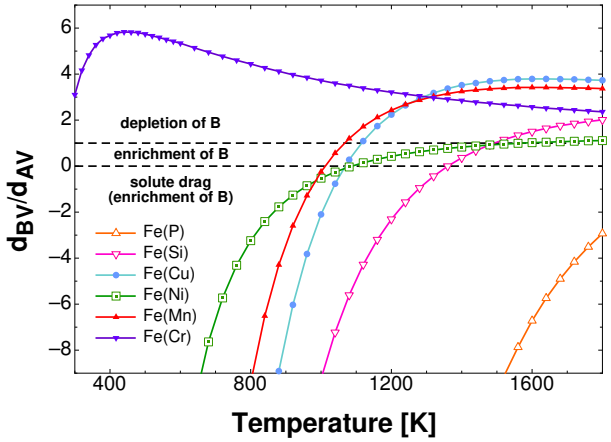

FIG. 7. RIS tendencies (Eq. 12) computed with the SCMF method in the 5nn model, for the Fe–X binary alloys. Solute drag (and subsequent enrichment at sinks) takes place when the ratio is negative; in the opposite case, enrichment holds as long as the ratio is smaller than 1.

at low temperatures and depletion at high temperatures, in agreement with the experimental trends observed in [3]. Furthermore, there exists a temperature interval in which the solute diffuses through the inverse Kirkendall mechanism, but since d_{BV} is smaller than d_{AV} the solvent atoms are moving away from the grain boundary and thus solute enhancement still occurs. An analogous trend is visible even in the Fe(Cr) system, but at such low temperatures it would never occur in reality.

In conclusion, as far as vacancy diffusion is concerned, all solutes except for Cr are expected to enrich at grain boundaries at RPV operational temperature, since they move through vacancy drag. At a relatively high temperatures, Cu and Mn switch from enrichment to depletion, while Ni, P and Si are always in the enrichment regime (the crossover for Si occurs above 1400 K). At any rate, the effective enrichment or depletion tendency has to be completed by adding the contribution given by interstitials and by the intrinsic diffusion coefficients appearing in Eq. 11.

CONCLUSIONS

The main goal of this study was to perform a systematic and complete analysis of transport and diffusion properties of 6 different solute species (Cr, Cu, Mn, Ni, P and Si) in bcc iron-based dilute alloys, with the aim of investigating flux coupling phenomena between solute species and monovacancies, in particular vacancy drag and RIS. A new multi-scale approach is developed, where DFT-computed jump frequencies are combined with a Self-Consistent Mean Field method that allows to correctly take into consideration longer-ranged solute-vacancy interactions.

It was shown that vacancy drag is a widespread phenomenon occurring systematically in real binary alloys characterized by non-negligible solute-vacancy interactions, i.e. all Fe(X) alloys except Fe(Cr). This result, especially in the case of Fe(Mn) and Fe(Ni), is in contrast with previous computations [22] based on the available multifrequency models, which are unsuitable for vacancy drag prediction as they do not treat correctly the crucial 2nn SVI. The drag strength is affected by the complex combined effect of thermodynamic and kinetic interactions. As a general trend, vacancy drag is stronger in the low temperature regime (< 1000 K), including RPV operational temperature (≈ 573 K), while the inverse Kirkendall mechanism is dominant at high temperature. The crossover temperature lies always close to or above the Curie temperature and is higher in those alloys where the SVI are stronger, whereas in the Fe(Cr) alloy the crossover occurs at room temperature. The results are supported by a very good agreement with Monte Carlo simulations and experimental solute tracer diffusion coefficients. Concerning the RIS profiles, all model alloys

with the exception of Fe(Cr) show the same trend: solute enrichment at low temperature and depletion at high temperature. This trend is in great agreement with the experiments performed in real multicomponent ferritic–martensitic alloys [3]; however, synergetic effects between solute atoms are here neglected. Depletion of Cr should occur if the only vacancy mechanism were in action. At any rate, the drag and RIS results are to be further investigated with the calculation of transport coefficients for interstitial–mediated diffusion, which is expected to be relevant in Fe(Cr), Fe(Mn) and Fe(P) [19, 35].

Since the drag character is strong at RPV temperature, it is likely that solute drag contributes to the formation of embrittling solute–defect clusters in RPV steels, although other diffusion mechanisms may also play a key–role (diffusion via single interstitials, small loops or voids). The described model represents a powerful tool for predicting diffusion properties. It combines accurate first principle calculations with the SCMF framework in order to obtain exact transport coefficients, especially in the low–temperature regime which is usually not accessible by experiments but is extremely important for many applications. The obtained sets of ab initio migration barriers represent as well a useful database for mean field modeling or AKMC simulations of ferritic steels.

ACKNOWLEDGMENTS

This work contributes to the Joint Programme on Nuclear Materials of the EERA. It was accomplished thanks to the financial support from Vattenfall AB, the Göran Gustafsson Foundation and the European Commission, in the framework of the MatISSE project under Grant No. 604862. The high performance computing resources were provided by the Swedish National Infrastructure for Computing (SNIC) centers PDC (Lindgren) and NSC (Triolith) and by the Swiss CSC resource ROSA through the PRACE–2IP project (FP7 RI–283493). Furthermore, the authors acknowledge L. Malerba, F. Soisson, N. Sandberg and Z. Chang for the valuable discussions.

* messina@kth.se

[1] F. Danoix, E. Bémont, P. Maugis, and D. Blavette, Adv. Eng. Mater. **8**, 1202 (2006).
[2] Z. Mao, C. K. Sudbrack, K. E. Yoon, G. Martin, and D. N. Seidman, Nat. Mater. **6**, 210 (2007).
[3] J. P. Wharry and G. S. Was, J. Nucl. Mat. **442**, 7 (2013).
[4] M. Nastar and F. Soisson, *Comprehensive Nuclear Materials* (Elsevier Inc., New York, 2012) Chap. 1.18, pp. 471–496.
[5] M. K. Miller, K. A. Powers, R. K. Nanstad, and P. Efsing, J. Nucl. Mat. **437**, 107 (2013).
[6] H. Hein, E. Keim, J. May, and H. Schnabel, in *IAEA Technical Meeting on Degradation of Primary Components of Pressurised Water Cooled Nuclear Power Plants: current issues and future challanges, 5-8 November 2013, Vienna, Austria* (2013).
[7] M. K. Miller and K. F. Russell, J. Nucl. Mat. **371**, 145 (2007).
[8] P. Auger, P. Pareige, S. Welzel, and J. C. Van Duysen, J. Nucl. Mat. **280**, 331 (2000).
[9] P. Efsing, C. Jansson, G. Embring, and T. Mager, J. ASTM Int. **4** (2007).
[10] S. C. Glade, B. D. Wirth, G. R. Odette, and P. Asoka-Kumar, J. Nucl. Mat. **351**, 197 (2006).
[11] Y. Nagai, K. Takadate, Z. Tang, H. Ohkubo, H. Sunaga, H. Takizawa, and M. Hasegawa, Phys. Rev. B **67**, 224202 (2003).
[12] K. Yabuuchi, M. Saito, R. Kasada, and A. Kimura, J. Nucl. Mat. **414**, 498 (2011).
[13] E. Meslin, B. Radiguet, and M. Loyer-Prost, Acta Mater. **61**, 6246 (2013).
[14] L. S. Darken, Trans. Aime **175**, 41 (1948).
[15] J. R. Manning, Metall. Mat. Trans. B **1**, 499 (1970).
[16] G. J. Ackland, M. I. Mendelev, D. J. Srolovitz, S. Han, and A. V. Barashev, J. Phys.: Condens. Matter **16**, S2629 (2004).
[17] E. Meslin, C.-C. Fu, A. Barbu, F. Gao, and F. Willaime, Phys. Rev. B **75**, 094303 (2007).
[18] D. A. Terentyev, L. Malerba, and M. Hou, Phys. Rev. B **75**, 104108 (2007).
[19] C. Domain and C. S. Becquart, Phys. Rev. B **71**, 214109 (2005).
[20] A. V. Barashev and A. C. Arokiam, Philos. Mag. Lett. **86**, 321 (2006).
[21] J. D. Tucker, R. Najafabadi, T. R. Allen, and D. Morgan, J. Nucl. Mat. **405**, 216 (2010).
[22] S. Choudhury, L. Barnard, J. D. Tucker, T. R. Allen, B. D. Wirth, M. Asta, and D. Morgan, J. Nucl. Mat. **411**, 1 (2011).
[23] A. R. Allnatt and E. L. Allnatt, Philos. Mag. A **49**, 625 (1984).
[24] A. D. Le Claire, J. Nucl. Mat. **69**, 70 (1978).
[25] P. Y. Serruys and G. Brebec, Philos. Mag. A **46**, 661 (1982).
[26] Y. Okamura and A. R. Allnatt, J. Phys. C: Solid State Phys. **16**, 1841 (1983).
[27] M. Nastar, V. Y. Dobretsov, and G. Martin, Philos. Mag. A **80**, 155 (2000).
[28] M. Nastar, Phil. Mag. **85**, 3767 (2005).
[29] V. Barbe and M. Nastar, Phil. Mag. **86**, 3503 (2006).
[30] V. Barbe and M. Nastar, Phil. Mag. **87**, 1649 (2007).
[31] T. Garnier, M. Nastar, P. Bellon, and D. R. Trinkle, Phys. Rev. B **88**, 134201 (2013).
[32] T. Garnier, D. R. Trinkle, M. Nastar, and P. Bellon, Phys. Rev. B **89**, 144202 (2014).
[33] A. Barbu and A. B. Lidiard, Philos. Mag. A **74**, 709 (1996).
[34] A. C. Arokiam, A. V. Barashev, D. J. Bacon, and Y. N. Osetsky, Phys. Rev. B **71**, 174205 (2005).
[35] P. Olsson, T. P. C. Klaver, and C. Domain, Phys. Rev. B **81**, 054102 (2010).
[36] G. H. Vineyard, J. Phys. Chem. Solids **3**, 121 (1957).
[37] L. Messina, Z. Chang, and P. Olsson, Nucl. Instrum. Methods Phys. Res. B **303**, 28 (2013).
[38] O. Senninger, E. Martínez, F. Soisson, M. Nastar, and Y. Bréchet, Acta Mater. **73**, 97 (2014).
[39] G. Kresse and J. Hafner, Phys. Rev. B **47**, 558 (1993).

[40] G. Kresse and J. Hafner, Phys. Rev. B **49**, 14251 (1994).
[41] G. Kresse and J. Hafner, J. Phys.: Condens. Matter **6**, 8245 (1994).
[42] P. E. Blöchl, Phys. Rev. B **50**, 17953 (1994).
[43] G. Kresse and D. Joubert, Phys. Rev. B **59**, 1758 (1999).
[44] J. P. Perdew, K. Burke, and Y. Wang, Phys. Rev. B **54**, 16533 (1996).
[45] S. H. Vosko, L. Wilk, and M. Nusair, Can. J. Phys. **58**, 1200 (1980).
[46] P. Olsson, C. Domain, and J. Wallenius, Phys. Rev. B **75**, 014110 (2007).
[47] G. Mills, H. Jonsson, and G. K. Schenter, Surf. Sci. **324**, 305 (1995).
[48] H. Jonsson, G. Mills, and K. W. Jacobsen, in *Classical and quantum dynamics in condensed phase simulations*, edited by B. J. Berne, G. Ciccotti, and D. F. Coker (World Scientific, 1998).
[49] G. Henkelman, B. P. Uberuaga, and H. Jonsson, J. Chem. Phys. **113**, 9901 (2000).
[50] D. Costa, *Modelling the thermal ageing evolution of Fe-Cr alloys using a lattice kinetic Monte Carlo approach based on DFT calculations* , Ph.D. thesis, Université de Sciences et Technologies USTL Lille 1 (2012).
[51] E. Vincent, C. S. Becquart, and C. Domain, J. Nucl. Mat. **351**, 88 (2006).
[52] P. Pulay, Chem. Phys. Lett. **73**, 393 (1980).
[53] G. P. Kerker, Phys. Rev. B **23**, 3082 (1981).
[54] Y. Mishin, M. R. Sörensen, and A. F. Voter, Philos. Mag. A **81**, 2591 (2001).
[55] T. Garnier, V. R. Manga, D. R. Trinkle, M. Nastar, and P. Bellon, Phys. Rev. B **88**, 134108 (2013).
[56] C. Kittel, *Introduction to Solid State Physics*, 8th ed. (Wiley, 2004).
[57] C. Domain, C. S. Becquart, and L. Malerba, J. Nucl. Mat. **335**, 121 (2004).
[58] C. Domain and C. S. Becquart, Phys. Rev. B **65**, 024103 (2001).
[59] F. Soisson and C.-C. Fu, Phys. Rev. B **76**, 214102 (2007).
[60] L. Malerba, G. J. Ackland, C. S. Becquart, G. Bonny, C. Domain, S. L. Dudarev, C. C. Fu, D. Hepburn, M. C. Marinica, P. Olsson, R. C. Pasianot, J. M. Raulot, F. Soisson, D. Terentyev, E. Vincent, and F. Willaime, J. Nucl. Mat. **406**, 7 (2010).
[61] G. Lucas and R. Schäublin, Nucl. Instrum. Methods Phys. Res. B **267**, 3009 (2009).
[62] R. D. Hatcher, R. Zeller, and P. H. Dederichs, Phys. Rev. B **19**, 5083 (1979).
[63] S. S. Pohlong and P. N. Ram, J. Phys.: Condens. Matter **10**, 10901 (1999).
[64] A. Seeger, Phys. Status Solidi A **167**, 289 (1998).
[65] H.-E. Schaefer, K. Maier, M. Weller, D. Herlach, A. Seeger, and J. Diehl, Scripta Metall. **11**, 803 (1977).
[66] L. De Schepper, D. Segers, L. Dorikens-Vanpraet, M. Dorikens, G. Knuyt, L. M. Stals, and P. Moser, Phys. Rev. B **27**, 5257 (1983).
[67] J. Wallenius, P. Olsson, C. Lagerstedt, N. Sandberg, R. Chakarova, and V. Pontikis, Phys. Rev. B **69**, 094103 (2004).
[68] A. Vehanen, P. Hautojärvi, J. Johansson, J. Yli-Kauppila, and P. Moser, Phys. Rev. B **25**, 762 (1982).
[69] A. Möslang, E. Albert, E. Recknagel, A. Weidinger, and P. Moser, Hyperfine Interact. **15**, 409 (1983).
[70] E. Vincent, C. S. Becquart, and C. Domain, Nucl. Instrum. Methods Phys. Res. B **228**, 137 (2005).
[71] O. I. Gorbatov, P. A. Korzhavyi, A. V. Ruban, B. Johansson, and Y. N. Gornostyrev, J. Nucl. Mat. **419**, 248 (2011).
[72] M. Doyama, Trans. Jpn. Inst. Met. **25**, 808 (1986).
[73] A. R. Allnatt and A. B. Lidiard, *Atomic Transport in Solids* (Cambridge University Press, 2003).
[74] A. Senhaji, G. Treglia, B. Legrand, N. T. Barrett, C. Guillot, and B. Villette, Surf. Sci. **274**, 297 (1992).
[75] E. Vincent, C. S. Becquart, and C. Domain, Nucl. Instrum. Methods Phys. Res. B **255**, 78 (2007).
[76] C. S. Becquart and C. Domain, Phys. Status Solidi B **247**, 9 (2010).
[77] Z. Chang, N. Sandberg, and P. A. Korzhavyi, private communication (2012).
[78] B. Jonsson, Z. Metallkd. **83**, 349 (1992).
[79] T. R. Anthony, in *Diffusion in Solids: Recent Developments*, edited by A. S. Nowick and J. J. Burton (Academic Press, New York, 1975) pp. 353–378.
[80] W. G. Wolfer, J. Nucl. Mat. **114**, 292 (1983).
[81] F. Soisson and C.-C. Fu, Solid State Phenom. **139**, 107 (2008).
[82] K. Hirano, M. Cohen, and B. L. Averbach, Acta Metall. **9**, 440 (1961).
[83] R. J. Borg and D. Lai, Acta Metall. **11**, 861 (1963).
[84] S. J. Rothman, J. Appl. Phys. **39**, 5041 (1968).
[85] A. W. Bowen and G. M. Leak, Metall. Trans. **1**, 2767 (1970).
[86] K. Nohara and K. Hirano, Proc. Int. Conf. Sci. Tech. Iron & Steel **7**, 11 (1970).
[87] V. Irmer and M. Feller-Kniepmeier, J. Phys. Chem. Solids **33**, 2141 (1972).
[88] J. S. Kirkaldy, P. N. Smith, and R. C. Sharma, Metall. Mat. Trans. B **4**, 624 (1973).
[89] G. Salje and M. Feller-Kniepmeier, J. Appl. Phys. **48**, 1833 (1977).
[90] G. Luckman, R. A. DiDio, and W. R. Graham, Metall. Trans. A **12A**, 253 (1981).
[91] T. Matsuyama, H. Hosokawa, and H. Suto, Trans. Jpn. Inst. Met. **24**, 589 (1983).
[92] D. Bergner, Y. Khaddour, and S. Lörx, in *Defect and Diffusion Forum*, edited by F. J. Kedves and D. L. Beke (1989) p. 409.
[93] J. Čermàk, M. Lübbehusen, and M. Mehrer, Z. Metallkd. **80**, 213 (1989).
[94] K. Hirano and Y. Iijima, in *Defect and Diffusion Forum*, edited by F. J. Kedves and D. L. Beke (1989) p. 1039.
[95] C. G. Lee, Y. Iijima, T. Hiratani, and K. Hirano, Mater. Trans., JIM **31**, 255 (1990).